LiDAR Aided Cycle Slip Detection for GNSS Real-time Kinematic Positioning in Urban Environments

Feng Huang, *Student Member*, Weisong Wen*, *Member*, Hoi-Fung Ng, and Li-Ta Hsu, *Senior Member, IEEE*

Abstract—Cycle slip of carrier-phase measurements is a common error source in global navigation satellite systems (GNSS) real-time kinematic (RTK) positioning. It limits the performance of the GNSS-RTK in urban canyons due to the excessive signal reflections from buildings. To fill this gap, this paper proposes a LiDAR-aided cycle slip detection method for GNSS-RTK, which benefits from the consecutive relative pose estimated by LiDAR odometry. Specifically, the difference between the triple-differenced carrier-phase measurements and that of prediction based on the LiDAR odometry is used to detect the potential cycle slips. The associated integer ambiguity is re-estimated if the cycle slip is observed to obtain an improved GNSS-RTK positioning. Experiments were conducted in a typical urban scenario of Hong Kong to verify the performance and effectiveness of the proposed method. The results demonstrated that the performance of the cycle slip can be effectively improved using the proposed method compared to the conventional loss of lock indicator (LLI) based method. Both the GNSS-RTK fixing rate and positioning accuracy can be improved by 17.33% and 13.86%, respectively with the help of the proposed LiDAR-aided method.

Keywords—Navigation; GNSS-RTK; LiDAR; Cycle Slip; Urban Canyons

I. INTRODUCTION

Global navigation satellite system (GNSS) [1] is a well-known approach for providing globally referenced positioning services for an autonomous system, such as the autonomous driving vehicle (ADV) [2] and autonomous aerial robots [3]. Existing GNSS positioning methods use the extended Kalman filter (EKF) [4] or factor graph optimization (FGO) [5] to estimate the position of the GNSS receiver which can only achieve the meter-level [6-8] accuracy by using the pseudorange and Doppler measurements. To improve the accuracy of GNSS positioning, GNSS-RTK is introduced to achieve centimeter-level positioning to meet the navigation requirements of the autonomous system [9]. Specifically, the GNSS-RTK technique eliminates systematic errors by adopting the double-differenced (DD) operation [4] between the observations received from a reference station and the one from the user. Ideally, centimeter-level accuracy can be achieved with the help of the high-resolution DD carrier-phase and pseudorange measurements in open areas once the integer ambiguities associated with the DD carrier-phase are correctly resolved, leading to the fixed solution. However, the positioning accuracy of the GNSS-RTK is significantly degraded in urban areas such as Hong Kong due to the excessive cycle slip [10] caused by the signal reflections from

buildings. Specifically, the estimation of the fixed solution for GNSS-RTK relies heavily on the integer ambiguity resolution. The resolved integer ambiguity is expected to be a constant and is used continuously [4]. Unfortunately, this assumption is violated once the cycle slip occurs. As a result, a significant error can be caused in GNSS-RTK if the cycle slip is not properly detected before the integer ambiguity resolution. Even if the cycle slip is one cycle, the range error is 19 centimeters [11] for global positioning system (GPS) L1 measurements. There are three major sources [12] of cycle slips. First of all, the cycle slips are caused by signal reflection due to the buildings, bridges, trees, etc., which are common elements in urban environments. Secondly, the cycle slip can suffer from signal-to-noise ratio (SNR) losses due to the multipath, satellite with low elevation angle, or high dynamics of the receiver. Third, false signal processing [13] might occurs because of the receiver software failure. In short, cycle slip detection is essential to achieving precise GNSS-RTK positioning in urban canyons.

To mitigate the impacts of the error raised by the cycle slip, numerous works [11, 13-15] were presented to distinguish the cycle slip. Essentially, the principles are similar. They try to use additional information or sensors to detect the inconsistency in the carrier-phase measurement. For example, Bisnath [13] and Gao [15] invested the DD observation in detecting the cycle slip based on the L1 and L2 observable combination using a typical dual-frequency GNSS receiver. In addition, Blewitt [16] proposed the TurboEdit method which uses undifferenced, dual-frequency carrier-phase data to identify the cycle slip. However, these methods are developed for dual frequencies that are not available for a single-frequency receiver. The code-phase difference, Doppler integration, and time-difference of carrier-phase can be used [17] to distinguish cycle slip in a single-frequency receiver. However, these methods have their limitation. The code-phase difference is difficult to detect small cycle slips because of the significant noise embedded in the code measurement. The Doppler observations are immune to cycle slips such that it is an option to detect the cycle slip [13] together with carrier measurements, but it cannot succeed in small cycle slips [11] and is affected by the multipath in urban scenarios. The time difference of carrier-phase also has unsatisfactory detection accuracy in high-dynamic conditions such as autonomous applications. In short, the accuracy of cycle slip detection for the small cycle slips and high receiver dynamic is limited.

To address the limitations, some researchers [18-21] integrate an inertial navigation system (INS) with a GNSS receiver to detect cycle slips. The INS can provide a high-

Feng Huang, Weisong Wen, Hoi-Fung Ng and Li-Ta Hsu are with the Hong Kong Polytechnic University, Hong Kong (correspondence e-mail: welson.wen@polyu.edu.hk). Weisong Wen is also with The Hong Kong Polytechnic University Shenzhen Research Institute.

frequency relative position by integrating its acceleration and rotation measurements based on the previous position from the GNSS system. The geodetic range between the satellite and the INS-predicted state is compared with the carrier-phase measurement to determine the probability of cycle slips. However, an automobile-level INS might not be sufficient as the performance of the INS relies on the correction of the internal bias[22] of the accelerometers and gyroscopes. In short, those methods rely heavily on the cost of the INS.

Recently, the LiDAR sensor has been widely used for autonomous systems and can provide accurate and high-frequency LiDAR odometry (LO) [23]. The LO method estimates the state by accumulating the relative transformation between consecutive frames. Our previous work [24] has proven that the LiDAR sensor can provide accurate relative state estimation in urban areas. Inspired by this, this work proposes to detect the cycle slip using the time-differenced carrier-phase with the help of LiDAR odometry. The precise LiDAR pose estimation is used to estimate the relative motion of the GNSS receiver. Then the cycle slip detection is conducted using the consecutive epochs of LiDAR-predicted ranges and the one from the received carrier-phase measurements. After the cycle slip is detected, the integer ambiguity will be re-estimated to get a fixed solution of GNSS-RTK. The remainder of the paper is laid out as follows: Section II presents the overview of the proposed LiDAR-aided cycle slip detection. The pose estimation based on the LiDAR odometry is given in Section III before elucidating the LiDAR-aided cycle slip detection in Section IV. Then, the performance evaluation is conducted in Section V. Finally, the conclusions are remarked, and future work is summarized.

II. OVERVIEW OF THE PROPOSED METHOD

The overview of the proposed framework is illustrated in Fig. 1. The pipeline mainly contains two parts: (1) the predicted state based on LiDAR odometry and orientation by attitude and heading reference system (AHRS) [25] and (2) the cycle slip detection based on the time difference of the DD carrier-phase and DD LiDAR-derived ranges. The difference between two DDs over different epochs is so-called a triple difference. In general, the purpose of using the tripe-difference method is to eliminate all systematic errors. Note that the relative pose estimation concerning the LiDAR local frame should be transformed into the GNSS global frame before its utilization in cycle slip detection. To this end, this paper directly adopts the orientation from the AHRS. Specifically, the inputs of the system include the point cloud from the LiDAR sensor, the orientation from the AHRS, and the raw measurements from the GNSS receiver and the reference station. The pose estimated by LiDAR odometry is aligned into the earth-centered, earth-fixed (ECEF) frame, corresponding to the light-blue boxes in Fig. 1 which will be discussed in Section III. Then the cycle slip is detected based on the difference between the triple-differenced carrier-phase measurements and that of prediction by the LiDAR odometry, corresponding to the light-yellow boxes in Fig. 1, which will be presented in Section IV. At last, the ambiguity is re-estimated to achieve a fixed solution.

The contributions of the work are summarized as follows:

(1) This paper proposes a LiDAR-aided approach to detect cycle slips in the triple-differenced carrier-phase measurements. We resolve the integer ambiguity resolution after detecting the potential cycle slips.

(2) Performance evaluation of the proposed pipeline using the challenging dataset collected in typical urban canyons of Hong Kong is presented. We verify the effectiveness of the proposed method step by step by comparing it with the conventional methods.
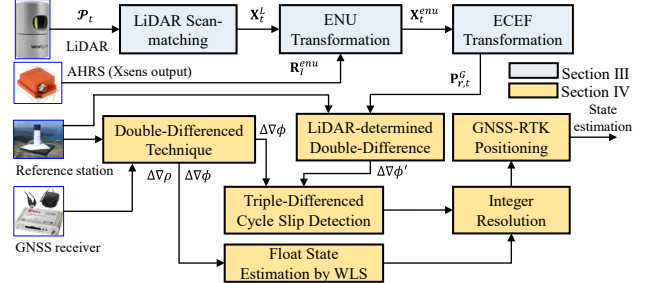

Fig. 1 Framework of the LiDAR-aided cycle slip detection. WLS denotes the weighted least squares method. The notations are explained in Table I.

TABLE I.   Notations and Definitions

Symbol	Description
t	The GNSS epoch at timestamp t
s	Index of satellite
r	The GNSS receiver
b	The reference station
ρ	Pseudorange measurement
ϕ	Carrier-phase measurement
ϕ'	The predicted range measurement
$\Delta\nabla\rho, \Delta\nabla\phi, \Delta\nabla\phi'$	Double-differenced pseudorange, carrier-phase, and predicted range, respectively
$\rho_{r,t}^s, \phi_{r,t}^s, \rho_{b,t}^s, \phi_{b,t}^s$	Pseudorange and carrier-phase received from satellite s to the receive and reference station at epoch t, respectively
G	ECEF frame
L	LiDAR body reference frame, which is fixed at the optical center of the sensor, normally is a superscript
I	AHRS body reference frame, normally is a superscript
enu	East, North, Up (ENU) frame
$\mathbf{P}_t^s, \mathbf{P}_{r,t}^G$	The position of the satellite s and receiver at timestamp t in the ECEF frame, respectively
$\mathcal{P}_t$	The point cloud received by the LiDAR sensor at timestamp t
$\mathbf{R}_l^{enu}$	The rotation matrix from AHRS body frame to ENU frame
$\mathbf{T}_1^2$	The transformation from frame 1 to frame 2, $\mathbf{T}_1^2 = [\mathbf{R}_1^2 \quad \mathbf{t}_1^2]$, which $\mathbf{R}_1^2$ and $\mathbf{t}_1^2$ denotes the rotation and translation, respectively.
$\mathbf{X}_t^{(.)}$	The state estimation at epoch t in the specified (.) frame, e.g., $\mathbf{X}_t^L$ denotes the state in the LiDAR frame. $\mathbf{X}_t^{(.)} = [\mathbf{R}_t^{(.)} \quad \mathbf{t}_t^{(.)}]$, which $\mathbf{R}_t^{(.)}$ and $\mathbf{t}_t^{(.)}$ denotes the rotation and translation, respectively.

To clarify the proposed pipeline, commonly used notations are defined in Table I and followed by the remainder of the paper. The state of the LiDAR odometry is denoted in the LiDAR local frame, which is fixed at the starting point. The positions of the GNSS receiver and satellites are in the ECEF frame.

III. STATE ESTIMATION BASED ON LiDAR ODOMETRY

This section presents the methodology of LiDAR odometry and the transformation between the LiDAR c and the

ECEF frame. The work in [26] has proved that low drift state estimation can be obtained by LiDAR odometry in urban environments.

A. LiDAR Odometry

LiDAR measures the range distance between the LiDAR sensor and the surrounding objects. As there is rich geometry information in urban areas, LiDAR odometry can extract a set of useful features from the raw point cloud. The m indicates the channel number of point cloud $\mathcal{P}_k$. $\mathbf{x}_{(k,i)}$ represents the i-th point in $\mathcal{P}_k$. $\mathbf{S}_{(k,i)}^m$ be a set of neighboring points of $\mathbf{x}_{(k,i)}$ in scan channel m. The feature points are extracted according to the smoothness of $\mathbf{x}_{(k,i)}$ and its consecutive points [26],

$$c_i = \frac{1}{N_s * \|\mathbf{x}_{(k,i)}\|} \left\| \sum_{j \in \mathbf{S}_{(k,i)}^m, j \neq i} \left(\mathbf{x}_{(k,i)} - \mathbf{x}_{(k,j)} \right) \right\| \quad (1)$$

where the $\mathbf{x}_{(k,j)}$ indicates the successive point of $\mathbf{x}_{(k,i)}$ within $\mathbf{S}_{(k,i)}^m$. N_s denotes the amount of points in $\mathbf{S}_{(k,i)}^m$, including $\mathbf{x}_{(k,i)}$ and successive points. The operator $\|*\|$ denotes the L2 norm. A point is classified as the edge feature with a large curvature value or is classified as a planar feature by a slight curvature value. The extracted features are registered with previously constructed feature mapping, so-called scan-to-matching. A more detailed description of the LiDAR odometry can be found in [24, 26].

B. ECEF Transformation

Given the pre-calibrated extrinsic parameters among the LiDAR, AHRS, and GNSS receiver, the LiDAR pose in the LiDAR frame can be converted to the receiver pose in the ENU frame as follows,

$$\mathbf{X}_{r,t}^{enu} = \begin{bmatrix} \mathbf{R}_I^{enu} & 0 \\ 0 & 1 \end{bmatrix}_{4 \times 4} \mathbf{T}_I^r \mathbf{T}_L^I \mathbf{X}_t^L \quad (2)$$

where the $\mathbf{T}_L^I$ is extrinsic to transform the pose from LiDAR frame to AHRS frame. $\mathbf{T}_I^r$ is the extrinsic parameter between the AHRS and the antenna of the GNSS receiver. $\mathbf{R}_I^{enu}$ is obtained by AHRS orientation estimation.

The origin of the ECEF domain is the center of mass of the earth in WGS 84 [27] ellipsoid. To transform from ENU to ECEF coordinate, a reference point of the ENU is required. The first fixed solution $\mathbf{P}_{fix}^G$ which is resolved by RTK-GNSS is selected as the reference location of the ENU coordinate. The state in the ENU frame can be converted to the ECEF frame following [1],

$$\mathbf{P}_{r,t}^G = \begin{bmatrix} -sin\lambda & -sin\phi cos\lambda & cos\phi cos\lambda \\ cos\lambda & -sin\phi sin\lambda & cos\phi sin\lambda \\ 0 & cos\phi & sin\phi \end{bmatrix} tran(\mathbf{X}_{r,t}^{enu}) + \mathbf{P}_{fix}^G (3)$$

where the ϕ and λ denote geodetic latitude and longitude of the reference point, respectively. Note that the first point is selected as the reference point in this paper. The operator $tran(*)$ is defined to get the translation of the state.

IV. LiDAR-Aided Cycle Slip Detection

A. Cycle Slip Detection Aided by LiDAR sensor

A carrier-phase measurement in units of length from the GNSS receiver can be expressed as [28],

$$\phi_{r,t}^s = r_{r,t}^s + c(\delta_{r,t} - \delta_{r,t}^s) - I_{r,t}^s + T_{r,t}^s + \lambda^s N_{r,t}^s + \varepsilon_{r,t}^s \quad (4)$$

where the λ^s represents the carrier wavelength of the corresponding GNSS signal. $r_{r,t}^s$ denotes the range distance between satellite and GNSS receiver. c denotes the speed of the light. $\delta_{r,t}$ and $\delta_{r,t}^s$ represent the receiver clock bias and the satellite clock bias, respectively. $I_{r,t}^s$ and $T_{r,t}^s$ represent the delay due to ionospheric and tropospheric layers, respectively. $N_{r,t}^s$ denotes the integer ambiguity value of carrier-phase. $\varepsilon_{r,t}^s$ denotes the unmodeled error such as receiver thermal noise and multipath.

The overview of DD carrier-phase measurement is shown in Fig. 2. The single difference between the receiver and base station with the common master satellite eliminates the satellite bias, ionospheric and tropospheric effects. Typically, the satellite with the highest elevation angle is chosen as the master satellite which is followed in this paper. Then, the receiver clock bias can be further eliminated by between-satellites single difference. The DD carrier-phase measurement for GNSS-RTK is denoted as follows [4],

$$\Delta\nabla\phi_{r,t}^s = (\phi_{r,t}^s - \phi_{b,t}^s) - (\phi_{r,t}^w - \phi_{b,t}^w)$$
$$= \Delta\nabla r_{r,t}^s + \lambda\Delta\nabla N_{r,t}^s + \Delta\nabla\varepsilon_{r,t}^s \quad (5)$$

where the satellite w represents the master satellite selected with the highest elevation angle. $\Delta\nabla N_{r,t}^s$ denotes the DD ambiguity which is to be resolved before obtaining the fixed solution. $\Delta\nabla\varepsilon_{r,t}^s$ indicates the noise associated with the DD carrier-phase measurements.

Given the LiDAR-predicted receiver pose in the ECEF frame which is derived in Section III-B, the range distance for satellite s to the receiver is computed as,

$$\phi'^s_{r,t} = \| \mathbf{P}_t^s - \mathbf{P}_{r,t}^G \|$$
$$= \sqrt{(P_{t,x}^s - P_{r,t,x}^G)^2 + (P_{t,y}^s - P_{r,t,y}^G)^2 + (P_{t,z}^s - P_{r,t,z}^G)^2} \quad (6)$$

where the $\phi'^s_{r,t}$ is the LiDAR-determined range distance between satellite and receiver. $\|*\|$ denotes the L2 vector norm [29]. $\mathbf{P}_t^s = (P_{t,x}^s, P_{t,y}^s, P_{t,z}^s)$ and $\mathbf{P}_{r,t}^G = (P_{r,t,x}^G, P_{r,t,y}^G, P_{r,t,z}^G)$ are the position of the satellite and the receiver in the ECEF frame, respectively. Therefore, the predicted DD range measurement aided by LiDAR sensors can be expressed as,

$$\Delta\nabla\phi'^s_{r,t} = (\phi'^s_{r,t} - \phi'^s_{b,t}) - (\phi'^w_{r,t} - \phi'^w_{b,t}) \quad (7)$$

Fig. 2 presents the difference of DD carrier-phase measurement, so-called the triple difference measurements, between two successive epochs, which can be expressed as,

$$\delta\Delta\nabla\phi_{r,t}^s = \Delta\nabla\phi_{r,t}^s - \Delta\nabla\phi_{r,t-1}^s$$
$$= \Delta\nabla r_{r,t}^s - \Delta\nabla r_{r,t-1}^s + \lambda(\Delta\nabla N_{r,t}^s - \Delta\nabla N_{r,t-1}^s) + \delta\Delta\nabla\varepsilon_{r,t}^s \quad (8)$$

$\delta\Delta\nabla\varepsilon_{r,t}^s$ indicates the changing of the unmodeled DD error between consecutive epochs.

Similarly, the time-differenced LiDAR-predicted range can be presented as,

$$\delta\Delta\nabla\phi'^s_{r,t} = \Delta\nabla\phi'^s_{r,t} - \Delta\nabla\phi'^s_{r,t-1} \quad (9)$$

In view of the fact that the LiDAR odometry can provide a highly accurate relative motion between two epochs with a

short time difference, the $\Delta\nabla r_{r,t}^s$ should equal to $\Delta\nabla\phi'^s_{r,t}$. The difference between $\delta\Delta\nabla\phi^s_{r,t}$ and $\delta\Delta\nabla\phi'^s_{r,t}$ can be denoted as,

$$d^s_{\delta\phi,t} = \delta\Delta\nabla\phi^s_{r,t} - \delta\Delta\nabla\phi'^s_{r,t} = \lambda(\Delta\nabla N^s_{r,t} - \Delta\nabla N^s_{r,t-1}) \quad (10)$$

where the $d^s_{\delta\phi,t}$ refers to the difference between the triple-differenced carrier-phase measurements and LiDAR-predicted range measurements, so-called DCL. If the carrier-phase measurement is free of cycle slips, the double-differenced ambiguity $\Delta\nabla N^s_{r,t}$ remains constant for the consecutive epochs. As a result, the DCL residual should be small if there is no cycle slip. Therefore, (10) can be used to detect cycle slips if $d^s_{\delta\phi,t}$ exceeding an experimentally determined threshold T_{DCL},

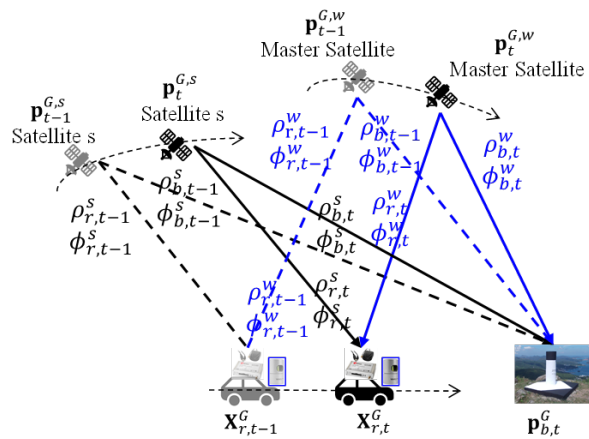$$\left| d^s_{\delta\phi,t} \right| > T_{DCL} \quad (11)$$

Fig. 2 Illustration of triple-differenced carrier-phase measurements.

B. GNSS-RTK Positioning Aided by Cycle Slip Detection

The float state estimation and carrier-phase integer ambiguity resolution are two main steps in GNSS-RTK positioning. In the first step, the float solution is estimated by the weighted least squares (WLS) [4]. Secondly, the integer ambiguity resolution (AR) is performed using the least-squares ambiguity decorrelation adjustment (LAMBDA) [30] algorithm in the second stage. If a cycle slip occurs, the AR needs to be resolved again to get a fixed solution. The implementation of the GNSS-RTK positioning is based on RTKLIB [4].

Cycle slip detection using LLI: The receiver provides an LLI indicator representing the status of the cycle slips. According to the Receiver Independent Exchange Format (RINEX) 3.03 [31], 3 bits are assigned to the cycle slips detection. If bits are set to 0 or blank, it means no cycle slip or not known. The possibility of a cycle slip is detected when bit 0 is set, while bit 1 is set when the existence of a half-cycle ambiguity or slip. In addition, the occurrence of a BOC-tracking of an MBOC-modulated signal if the LLI is set to bit 2 [31]. The measurements are marked with a cycle slip by LLI easily due to the signal reflections from buildings in urban environments.

V. EXPERIMENT RESULTS AND DISCUSSIONS

A. Experiment Setup

To validate the performance of the proposed LiDAR-aided cycle slip detection method, the experiment is conducted in typical urban environments in Hong Kong using our open-sourced *UrbanNav* [32] datasets. The datasets contain measurements from multi-GNSS receivers, INS, cameras, and multi-LiDARs. Besides, the ground truth (GT) positioning is obtained by NovAtel SPAN-CPT, which integrates fiber optics gyroscope (FOG) into the GNSS-RTK, as shown in Fig. 3. Furthermore, we post-process the GT from SPAN-CPT using the state-of-the-art NovAtel Inertial Explorer [33] software to maximizes the accuracy of the trajectory.

In this experiment, a commercial u-box F9P GNSS receiver was employed to collect the raw measurement of GPS/Beidou at 1 Hz. The LiDAR frame rate is 10 Hz. In addition, the GNSS time and LiDAR timestamp is hardware synchronized [32] during the data collection. Meanwhile, the extrinsic parameters of the GNSS receiver, LiDAR sensor, and NovAtel SPAN-CPT were calibrated in advance.

The datasets are processed with a desktop and the specification is provided as below:
- An AMD Ryzen 5950X CPU with 16 cores, 32 threads
- 2 x 32GB DDR4 3600 MHz RAM Memory

Fig. 3 *Left*: Setup for the sensor platform. A u-blox F9P, Velodyne HDL-32E 3D LiDAR, and ground truth positioning provided by SPAN-CPT are adopted during the evaluation. *Right*: The typical urban environment of Hong Kong to be evaluated.

B. Evaluation Metrics and Methods

1) Cycle Slip Ground Truth Labeling

To verify the effectiveness of the proposed cycle slip detection, we use the ground truth positioning provided by NovAtel SPAN-CPT to label the cycle slip. In other words, relative pose from the ground truth estimation is adopted to replace the role of the LiDAR odometry in (8).

Specifically, the range measurement between the satellite and the receiver at epoch *t* can be derived following (6) after applying the transformation from the SPAN-CPT to the antenna of the receiver. Furthermore, the triple-difference GT-based range measurement can be computed based on the DD range measurement using consecutive epochs.

Recall (8), the difference $d^s_{\delta\phi,gt,t}$ between the triple-differenced carrier-phase $\delta\Delta\nabla\phi^s_{r,t}$ and GT-based range measurement $\delta\Delta\nabla r^s_{r,t}$ can be expressed as follows,

$$d^s_{\delta\phi,gt,t} = \delta\Delta\nabla\phi^s_{r,t} - \delta\Delta\nabla r^s_{r,t}$$
$$= \lambda(\Delta\nabla N^s_{r,t} - \Delta\nabla N^s_{r,t-1}) \quad (12)$$

$d^s_{\delta\phi,gt,t}$ can be used to label the cycle slips when the threshold is exceeded.

2) Performance Evaluation of the GNSS-RTK Cycle Slip Detection

In this paper, the performance evaluation of the LiDAR-aided GNSS-RTK cycle slip detection is based on the results of cycle slip ground truth labeling in the previous section. We only evaluate the data epochs in which DD measurements exist in the consecutive epochs because the ground truth labeling of the cycle slips is based on the triple-differenced measurements. The accuracy of the cycle slip detection can be defined as,

$$P_{dr} = \frac{N_{cs} \cap N_{gt}}{N_{gt}} \qquad (13)$$

where the P_{dr} denotes the percentage of detection rate. The N_{cs} denotes the amount of cycle slip satellites detected using the proposed method. The N_{gt} denotes the number of cycle slip satellites detected using the ground truth labeling in Section V-B. The higher value of the P_{dr} means the larger overlapping level of the cycle slip detection and GT labeling.

To validate the contributions of the proposed method in cycle detection, the following methods are evaluated,

(1) **LLI:** The cycle slips are marked by the LLI flags.
(2) **LAD:** The proposed LiDAR-aided (LA) cycle slip detection scheme.

3) Performance Evaluation of the GNSS-RTK Positioning

The fixed solution is resolved using the raw measurements of the GNSS receiver from the user (rover) and the GNSS receiver from the base station via RTKLIB [4]. The setting for RTKLIB evaluation is shown in Table II:

TABLE II. Process Setting in RTKLIB

Parameter	Value	Parameter	Value
Positioning Mode	Kinematic	Satellite System	GPS/Beidou
Ionosphere Model	Broadcast	Frequency	L1
Troposphere Model	Saastamoinen Model	Elevation Mask	15 degrees
Integer Ambiguity Resolution	Fix and Hold	Ephemeris	Hong Kong Land Department
Min Ratio to Fix Ambiguity	3.0	Filter Type	Forward

Meanwhile, the availability and fixing rate of GNSS-RTK are defined for better classification. The availability P_a is defined as the percentage of epochs N_{sol} where can be resolved by RTKLIB, divided by the total number of epochs N_{eph} in the GNSS measurement,

$$P_a = \frac{N_{sol}}{N_{eph}} \qquad (14)$$

The fixing rate P_{fix} is defined as the percentage of epochs where the integer fixed successfully N_{fix}, divided by the total number of epochs N_{sol},

$$P_{fix} = \frac{N_{fix}}{N_{sol}} \qquad (15)$$

To validate the contributions of the proposed method in this paper, we evaluate the following four methods,

(1) **RTKLIB**: The conventional GNSS-RTK positioning [4]

uses the LLI to detect the cycle slips. The ambiguity will be re-estimated if a cycle slip occurs.
(2) **RTK-LA:** The GNSS-RTK positioning with LiDAR-aided cycle slip detection only. The ambiguity will be re-estimated if a cycle slip occurs.
(3) **RTK-LAE:** The GNSS-RTK positioning method combines the detection of LiDAR-aided cycle slip and the LLI flags. LiDAR-aided Cycle slip detected satellite is excluded from the position estimation.
(4) **RTK-LAR:** The proposed GNSS-RTK positioning method combines the detection of LiDAR-aided cycle slip and the LLI flags. The estimated ambiguity is reset and refixed if a cycle slip is detected.

C. Experimental Validation in Urban Environments

The experiment is conducted in an urban area of Hong Kong near Kowloon Town with a total path of 675 m, and an example scenario is shown on the right side of Fig. 3. Numerous trees and buildings are involved such that it is a typical urban environment with many cycle slips occurred.

1) GNSS-RTK Cycle Slip Detection in Urban Areas

The results of the cycle slip detection using LLI and LiDAR-aided method are shown in Table III. The total number of cycle slips labeled by the ground truth is 104 out of 1235 measurements. The labeled cycle slips are 8.4% in this environment. 33 common-view measurements are marked from the 402 LLI slip detections according to the cycle slip ground truth labeling. The reason that other 369 LLI flags are not counted as cycle slip comparison is that cycle slip ground truth labeling computes successive carrier-phase measurements only. In other words, we do not consider the LLI flags from the unlabeled measurements. With the help of LiDAR odometry, RTK-LA observed 94.2% of cycle slips successfully while only 10.6% were identified by LLI flags. In addition, we observed that the number of cycle slips marked by LLI is quite large compared to the number of ground truth labels or LiDAR-aided method. The reason for this is that the cycle slips are produced and marked by LLI easily at the beginning of the signal tracking or the low SNR in urban areas.

TABLE III. Performance evaluation of cycle slip detection in the urban environment. $N_{cs} \cap N_{gt}$ indicates the number of cycle slip satellites detected both by the proposed method and the ground truth labeling in Section V-B. (num: number)

Results	Ground Truth Labeled	LLI	LAD
Num of Detection	104	402	105
Num of Correctly Detected, $N_{cs} \cap N_{gt}$	/	33	**98**
Detection Rate P_{dr}	/	10.6%	**94.2%**

Fig. 4 and Fig. 5 demonstrate the cycle slip detection results of G01 and C11, respectively. Most cycle slips can be distinguished based on the experimental threshold marked in red dash-dot with 0.57 m (3 cycles for L1 measurement). Interestingly, most of the LLI flags in G01 and C11 which are marked in the red box of Figs. 4 and 5 are detected at the beginning of the tracking or the discontinuous measurement in the urban environment. Meanwhile, RTK-LA methods can

detect the cycle slips in continuous measurement effectively. In short, the cycle slip detection of the LLI flags and the LiDAR-aided could be complementary for the GNSS-RTK positioning.
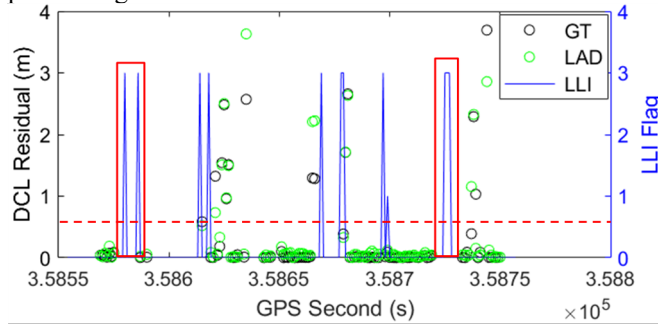

Fig. 4 The cycle slip detection result on satellite G01. The x-axis, left y-axis and right y-axis denote the GPS seconds, absolution value of DCL residual, and LLI flag, respectively. The red dash-dot line indicated the threshold (0.57 m) for cycle slips of DCL residuals.
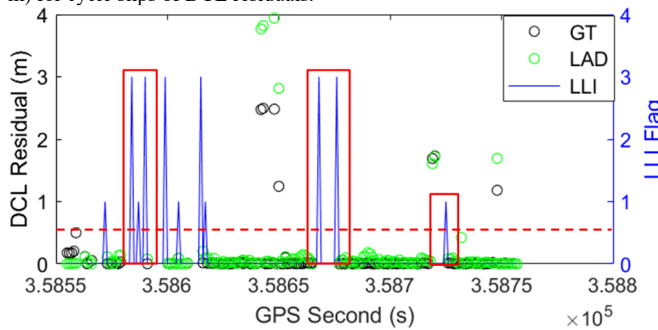

Fig. 5 The cycle slip detection result on satellite C11. The x-axis, left y-axis and right y-axis denote the GPS seconds, absolution value of DCL residual, and LLI flag, respectively. The red dash-dot line indicated the threshold (0.57 m) for cycle slips of DCL residuals.

2) GNSS-RTK Fixing rate and Positioning results in Urban Areas

To effectively evaluate the cycle slip detection of the LLI and LiDAR-aided methods, several positioning methods are evaluated to explore the combination of the LLI and the LiDAR-aided approaches. The results of the fixing rate using the four methods are shown in Table IV. The proposed RTK-LAR obtained a 25.25% fixing rate, the highest among the evaluated GNSS-RTK methods. Meanwhile, RTK-LA performs worse in terms of the fixing rate. The reason is that some carrier-phase measurements are discontinuous, thus affecting the usability of the proposed triple-differenced formulation. RTK-LAE retained a better performance by excluding the measurement from satellites with cycle slips. However, lower availability using RTK-LAE as it excludes all the measurements with the cycle slip excessively.

TABLE IV. Performance evaluation of GNSS-RTK in terms of fixing rate and 2D Position error.

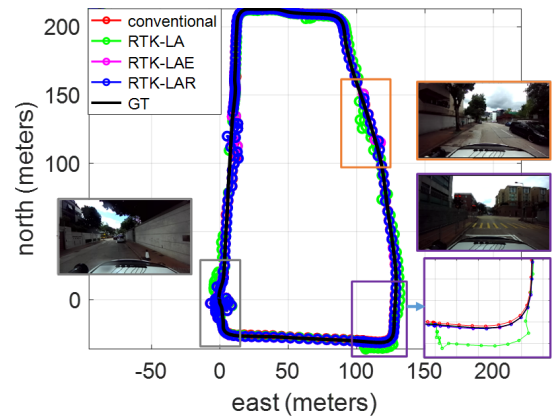| Results	RTKLIB	RTK-LA	RTK-LAE	RTK-LAR
Availability P_a	99.02%	99.02%	97.55%	**99.02%**
Fixing Rate P_{fix}	7.92%	3.96%	14.57%	**25.25%**
Improvement of Fixing Rate	/	-3.96%	6.65%	**17.33%**
MEAN (m)	1.298	2.715	1.173	**1.118**
STD (m)	2.459	3.590	2.451	**2.446**
Improvement of Positioning	/	/	9.64%	**13.86%**

Fig. 6 2D positioning trajectories of the four methods. The x-axis and y-axis denote the east and north directions, respectively. The black curve represents the ground truth positioning. The areas marked in grey, purple, and orange represent three typical urban areas, respectively.
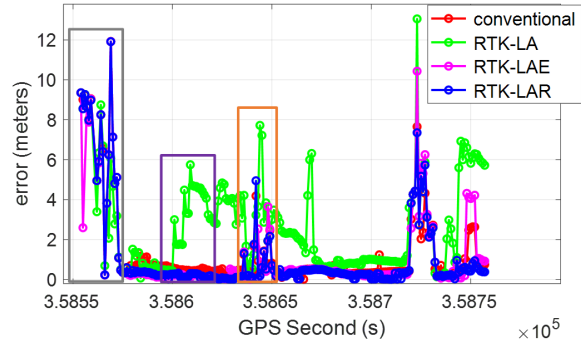

Fig. 7 2D positioning errors of the four methods. The x-axis and y-axis denote the epoch and 2D error, respectively. The areas marked in grey, purple, and orange represents the corresponding area in Fig. 6, respectively.

In terms of positioning accuracy, the RTK-LAR outperforms other methods with a mean error of 1.1178 m. The maximum error of the RTK-LA is worse than the other methods. 13.86% improvement of the mean positioning error is achieved by RTK-RTK compared to the conventional GNSS-RTK method as shown in Table IV.

Fig. 6 and Fig. 7 show the trajectories and the positioning error using four methods, respectively. The more accurate trajectory is estimated using RTK-LAR with the help of LiDAR-aided cycle slip detection, especially in the areas marked in Fig. 6. After applying the LiDAR-aided cycle slip detection, the positioning performance of GNSS-RTK is improved significantly in this urban area, especially in the purple and orange area in Fig.6 and Fig. 7. However, unsatisfactory positioning accuracy is observed in the grey area in Figs 6 and 7 due to excessive sign reflections. Therefore, it is important to integrate additional onboard sensors such as IMU to improve the performance of state estimation.

VI. CONCLUSION AND FUTURE WORK

Cycle slip is one of the key challenges in GNSS-RTK. Undetected cycle slips affect the fixing rate and the positioning accuracy in urban areas. Therefore, the detection of cycle slip is significant for improving the performance of GNSS-RTK. The paper proposes the cycle slip detection aided by the predicted triple-differenced range measurements using the LiDAR sensor and obtains a satisfactory solution in terms of fixing rate and state estimation in an urban area.

In the future, we will study the integration of LiDAR and GNSS-RTK to reduce the global drift of LiDAR for long-term autonomous driving systems. The GNSS-LiDAR-Inertial multi-sensor fusion [34, 35] is another interesting topic to reduce positioning error in urban areas.

ACKNOWLEDGMENT

REFERENCES

[1] P. D. Groves, *Principles of GNSS, inertial, and multisensor integrated navigation systems*. Boston: Boston : Artech House, 2008.

[2] P. Cai, Y. Sun, Y. Chen, and M. Liu, "Vision-based trajectory planning via imitation learning for autonomous vehicles," in *2019 IEEE Intelligent Transportation Systems Conference (ITSC)*, 2019: IEEE, pp. 2736-2742.

[3] S. Rajappa, M. Ryll, H. H. Bülthoff, and A. Franchi, "Modeling, control and design optimization for a fully-actuated hexarotor aerial vehicle with tilted propellers," in *2015 IEEE International Conference on Robotics and Automation (ICRA)*, 26-30 May 2015 2015, pp. 4006-4013, doi: 10.1109/ICRA.2015.7139759.

[4] T. Takasu and A. Yasuda, "Development of the low-cost RTK-GPS receiver with an open source program package RTKLIB," in *International symposium on GPS/GNSS*, 2009, vol. 1: International Convention Center Jeju Korea.

[5] W. Wen and L.-T. Hsu, "Towards robust GNSS positioning and Real-time kinematic using factor graph optimization," in *2021 IEEE International Conference on Robotics and Automation (ICRA)*, 2021: IEEE, pp. 5884-5890.

[6] A. Angrisano, S. Gaglione, and C. Gioia, "Performance assessment of GPS/GLONASS single point positioning in an urban environment," *Acta Geodaetica et Geophysica*, vol. 48, no. 2, pp. 149-161, 2013.

[7] W. Wen, T. Pfeifer, X. Bai, and L.-T. Hsu, "Factor graph optimization for GNSS/INS integration: A comparison with the extended Kalman filter," *NAVIGATION, Journal of the Institute of Navigation*, vol. 68, no. 2, pp. 315-331, 2021.

[8] H. F. Ng and L. T. Hsu, "3D Mapping Database-Aided GNSS RTK and Its Assessments in Urban Canyons," *IEEE Transactions on Aerospace and Electronic Systems*, vol. 57, no. 5, pp. 3150-3166, 2021, doi: 10.1109/TAES.2021.3069271.

[9] N. C. Talbot, "Centimeters in the field, a users perspective of real-time kinematic positioning in a production environment," in *Proceedings of the 6th International Technical Meeting of the Satellite Division of The Institute of Navigation (ION GPS 1993)*, 1993, pp. 1049-1057.

[10] B. Li, T. Liu, L. Nie, and Y. Qin, "Single-frequency GNSS cycle slip estimation with positional polynomial constraint," *Journal of Geodesy*, vol. 93, no. 9, pp. 1781-1803, 2019.

[11] Z. Liu, "A new automated cycle slip detection and repair method for a single dual-frequency GPS receiver," *Journal of Geodesy*, vol. 85, no. 3, pp. 171-183, 2011.

[12] D. Kim and R. B. Langley, "Instantaneous Real‐Time Cycle‐Slip Correction for Quality Control of GPS Carrier‐Phase Measurements," *Navigation*, vol. 49, no. 4, pp. 205-222, 2002.

[13] J. Zhao, M. Hernández-Pajares, Z. Li, L. Wang, and H. Yuan, "High-rate Doppler-aided cycle slip detection and repair method for low-cost single-frequency receivers," *GPS Solutions*, vol. 24, no. 3, p. 80, 2020/06/08 2020, doi: 10.1007/s10291-020-00993-0.

[14] S. B. Bisnath, "Efficient, automated cycle-slip correction of dual-frequency kinematic GPS data," in *Proceedings of the 13th International Technical Meeting of the Satellite Division of The Institute of Navigation (ION GPS 2000)*, 2000, pp. 145-154.

[15] R. Furukawa, N. Kubo, and A. El-Mowafy, "Prediction of RTK-GNSS performance in urban environments using a 3D model and continuous LoS method," in *Proceedings of the 2020 International Technical Meeting of The Institute of Navigation*, 2020, pp. 763-771.

[16] G. Blewitt, "An automatic editing algorithm for GPS data," *Geophysical research letters*, vol. 17, no. 3, pp. 199-202, 1990.

[17] G. Xu and Y. Xu, *GPS: theory, algorithms and applications*. Springer, 2016.

[18] T. Takasu and A. Yasuda, "Cycle slip detection and fixing by MEMS-IMU/GPS integration for mobile environment RTK-GPS," in *Proceedings of the 21st international technical meeting of the satellite division of the Institute of Navigation (ION GNSS 2008)*, 2008, pp. 64-71.

[19] C. Altmayer, "Enhancing the integrity of integrated GPS/INS systems by cycle slip detection and correction," in *Proceedings of the IEEE Intelligent Vehicles Symposium 2000 (Cat. No. 00TH8511)*, 2000: IEEE, pp. 174-179.

[20] M. O. Karaim, T. B. Karamat, A. Noureldin, M. Tamazin, and M. M. Atia, "Real-time cycle-slip detection and correction for land vehicle navigation using inertial aiding," in *Proceedings of the 26th international technical meeting of the satellite division of the institute of navigation (ION GNSS+ 2013)*, 2013, pp. 1290-1298.

[21] T. Li, H. Zhang, Z. Gao, Q. Chen, and X. Niu, "High-accuracy positioning in urban environments using single-frequency multi-GNSS RTK/MEMS-IMU integration," *Remote sensing*, vol. 10, no. 2, p. 205, 2018.

[22] X. Zhang, F. Zhu, Y. Zhang, F. Mohamed, and W. Zhou, "The improvement in integer ambiguity resolution with INS aiding for kinematic precise point positioning," *Journal of Geodesy*, vol. 93, no. 7, pp. 993-1010, 2019.

[23] M. Magnusson, A. Lilienthal, and T. Duckett, "Scan registration for autonomous mining vehicles using 3D‐NDT," *J Field Robot*, vol. 24, no. 10, pp. 803-827, 2007, doi: https://doi.org/10.1002/rob.20204.

[24] F. Huang, W. Wen, J. Zhang, and L. T. Hsu, "Point Wise or Feature Wise? A Benchmark Comparison of Publicly Available Lidar Odometry Algorithms in Urban Canyons," *IEEE Intelligent Transportation Systems Magazine*, pp. 2-20, 2022, doi: 10.1109/MITS.2021.3092731.

[25] W. Geiger *et al.*, "MEMS IMU for ahrs applications," in *Proceedings of IEEE/ION PLANS 2008*, 2008, pp. 225-231.

[26] J. Zhang and S. Singh, "Low-drift and real-time lidar odometry and mapping," *Autonomous Robots*, vol. 41, no. 2, pp. 401-416, 2017.

[27] J. A. Slater and S. Malys, "WGS 84—Past, present and future," in *Advances in positioning and reference frames*: Springer, 1998, pp. 1-7.

[28] E. D. Kaplan and C. Hegarty, *Understanding GPS/GNSS: principles and applications*. Artech house, 2017.

[29] G. A. Watson, "Characterization of the subdifferential of some matrix norms," *Linear algebra and its applications*, vol. 170, no. 0, pp. 33-45, 1992.

[30] P. J. G. Teunissen, "The least-squares ambiguity decorrelation adjustment: a method for fast GPS integer ambiguity estimation," *Journal of Geodesy*, vol. 70, no. 1, pp. 65-82, 1995/11/01 1995, doi: 10.1007/BF00863419.

[31] R.-S. IGS, "RINEX-The Receiver Independent Exchange Format (Version 3.03)," 2015.

[32] L.-T. Hsu *et al.*, "UrbanNav: An open-sourced multisensory dataset for benchmarking positioning algorithms designed for urban areas," in *Proceedings of the 34th International Technical Meeting of the Satellite Division of The Institute of Navigation (ION GNSS+ 2021)*, 2021, pp. 226-256.

[33] N. Inc., "Waypoint Inertial Explorer 8.80 Post Processing Software," 2019.

[34] J. Zhang, W. Wen, F. Huang, X. Chen, and L.-T. Hsu, "Coarse-to-Fine Loosely-Coupled LiDAR-Inertial Odometry for Urban Positioning and Mapping," *Remote Sensing*, vol. 13, no. 12, p. 2371, 2021.

[35] J. Zhang, W. Wen, F. Huang, Y. Wang, X. Chen, and L.-T. Hsu, "GNSS-RTK Adaptively Integrated with LiDAR/IMU Odometry for Continuously Global Positioning in Urban Canyons," *Applied Sciences*, vol. 12, no. 10, p. 5193, 2022.